ORIGINAL PAPER

Main control factors of coalbed methane occurrence differences in adjacent coal seams - a case study of Luling coal mine, Huaibei Coalfield, China

Siwen Zheng[1,2] · Liang Wang[1,2] · Dapeng Chen[1,2] · Yuanyuan Liu[1,2] · Changbao Jiang[3]

Abstract

Coalbed methane (CBM) is a natural gas resource related with coal deposits. In general, Gas status parameters gradually with the depth of the stratum. However, in areas with complex geological structures and multiple coal seam occurrences, the gas storage situation in shallow coal seams is typically better than in deep coal seams. This research paper focuses on coal seams numbered 8, 9, and 10 within the Luling coal seam as the subject of study. The study combines the analysis of gas accumulation history, laboratory experiments, and field investigations to examine the differences in gas occurrence within the coal seam group. The findings suggest that the differences in gas occurrence state within each coal seam of the Luling coal mine is predominantly governed by tectonic processes. During the process of tectonic evolution, the thicker coal seams, such as Nos. 8 and 9, are more prone to fracturing, leading to the formation of widely distributed tectonic coal. These broken coal bodies exhibit a significant capacity to store gas, resulting in favorable gas storage conditions within these coal seams. On the other hand, the low permeability of the mudstone in the roof layer restricts the migration and seepage of gas in the No. 10 coal seam, leading to a comparatively lower sealing effect for gas. By providing a comprehensive understanding of the gas content differences in the coal seam group, this study highlights the significant influence of geological processes on the distribution and storage of gas. These findings contribute to understanding the characteristics of gas reservoirs under complex geological conditions and adopting corresponding measures to reduce the risk of coal and gas outbursts in coal seams.

Keywords Geological structure · Gas occurrence · Tectonic coal · Paleogeography

✉ Liang Wang
  wangliang@cumt.edu.cn

1   Key Laboratory of Gas and Fire Control for Coal Mines (China University of Mining and Technology), Ministry of Education, Xuzhou 221116, China

2   National Engineering Research Center for Coal & Gas Control, China University of Mining and Technology, Xuzhou 221116, China

3   State Key Laboratory of Coal Mine Disaster Dynamics and Control, Chongqing University, Chongqing 400030, China

1 Introduction

Coalbed methane (CBM) is a valuable resource that is found in association with coal, primarily stored in both adsorbed and free states. Leakage of gas from coal seams contributes to the greenhouse effect (Bustin and Clarkson 1998; Qin et al. 2018), and more significantly, accidental gas release during coal mining operations can lead to hazardous events such as coal and gas outbursts and gas explosions (Wang and Cheng 2023). Therefore, accurately understanding the gas accumulation patterns in coal seams under different geological conditions is crucial for precise management of coal seam gas and ensuring safe production in coal mines. Additionally, the utilization of extracted coal bed methane not only helps mitigate greenhouse gas emissions but also presents an opportunity for economic value generation (Liu et al. 2019; Moore 2012).

The protective layer measure is a gas management method that capitalizes on the variation in gas storage among different coal seams within a coal seam group. It involves selectively mining the low-gas seams (protected seams) to release the gas in the neighboring high-gas coal seams (Kong et al. 2014). Hence, understanding the gas storage characteristics under varying coal seam group conditions is pivotal for employing this measure effectively. Typically, within the same geological unit, the gas status parameters of coal seams tends to increase with depth (Wang et al. 2012). Consequently, the upper protective layer measure is extensively utilized in most Chinese mining areas. However, as mining progresses deeper into more complex geological conditions, anomalies in gas storage become more prevalent. This is evidenced by the higher gas content observed in shallow coal seams compared to deeper coal seams, leading to a significant number of cases where the lower protective layer project is employed, particularly in the Huainan and Huaibei mines in China (Cheng et al. 2020; Wang et al. 2013). Therefore, understanding the reasons and primary controlling factors leading to variations in the gas occurrence, and implementing gas management measures tailored to the characteristics of coalbed gas occurrence, can significantly reduce gas accidents and enhance gas management efficiency.

Coal seams naturally release gas to achieve equilibrium with the geological and physical conditions of the formation site. Several factors contribute to the variation in gas storage within coal seams. Thicker hydrocarbon source rocks have the potential to generate larger quantities of stable natural gas, which is favorable for gas storage in the reservoir (Zhu et al. 2012). Additionally, the development of cracks in the top plate of coal seams and the lithology of the top plate influence gas storage (Karacan and Goodman 2012). In addition to the thickness of coal seam itself and the properties of surrounding rock, the change of external environment also affects the occurrence of gas in this coal seam. The regional structure and hydrogeology play crucial roles in gas storage (Pashin 2007). Open positive faults facilitate the escape of groundwater and gas, thereby reducing the gas content in the reservoir (Karacan et al. 2011; Su et al. 2003). Research has shown that volcanic activity can release significant amounts of gas from the coalbed into the atmosphere, as observed through chemical composition and isotope analysis of methane associated with volcanic activity (Zheng et al. 2017). Gas storage characteristics have also been studied in the context of coal seam clusters. Some researchers have noted higher production in shallow reservoirs containing fresh water compared to deep, low-permeability reservoirs containing saltwater (Pashin 2007). This difference is attributed to hydraulic confinement between distinct gas-bearing systems, resulting in significant variations in gas storage (Qin et al. 2018). While existing studies

focus on analyzing different gas-bearing systems based on the storage environment, limited research has been conducted on analyzing differences within the same gas-bearing system. Furthermore, the influence of the coal seam's own transformation on gas storage differences has not been extensively explored.

In this study, the Luling coal mine was investigated as a representative case to examine the negative correlation between gas content characteristics of coal seam groups and depth. The research focused on coal seam groups deposited during the Carboniferous-Permian period in the North China coal accumulation basin. The research aimed to analyze various properties of the coal in Luling Coal Mine, including its coal forming period, functional group composition, pore fracture characteristics, and fracture characteristics of tectonic coal. To achieve this, experimental methods such as carbon isotope analysis, infrared spectroscopy, scanning electron microscopy, physical adsorption instruments, electromagnetic vibrating screens, and laser particle size analyzers were employed. In addition to the experimental analysis, the study also utilized existing geological data and considered the development degree of tectonic coal in Luling coal mine to establish a reservoir forming event map of the gas system in the area. By combining this information with the study of the coal seam's internal structure and its sedimentary evolution history, the reasons behind the differences in gas content within the coal seam groups could be revealed. The results of this research provide important insights for the exploration and exploitation of gas in the study area and similar basins.

2 Geological setting and distribution characteristics of CBM

The Huaibei coal-gathering basin, located in the southern part of the North China block, is a significant coalfield in China (Fig. 1 (a)). It spans a broad area, stretching from the western Xiayi-Fuyang fault to the eastern Tanlu fault, and from the northern Fengpei fault to the southern Taihe-Guzhen fault. The regional structure of the area is intricate and influenced by the evolution of both internal and edge structures of tectonic plates. The primary structural patterns observed in the area are the east-west (EW) and north-northeast (NNE) trends. The complex structural configuration in the Huaibei coalfield is a result of multiple stages of tectonic movements. The NNE trending structure has transformed the earlier EW trending structure, leading to the formation of a crisscross network fault structure. This multi-stage tectonic evolution has contributed to the intricate fault system observed in the coalfield (Jiang et al. 2010).

The Luling coal mine is located southwest of the south Suzhou syncline (Fig. 1(b)). The mine mainly mines Nos. 8, 9 and 10 coal seams, and does not mine No. 7 coal seam. These coal seams were formed during the Permo-Carboniferous coal accumulation period. It is worth noting that the Nos. 8 and 9 coal seams are situated above the No. 10 coal seam (Fig. 1(f)).

2.1 Geological structure

The study area exhibits various fold structures including the east Suzhou syncline, Xiaoshijia anticline, Songjingwang anticline, and Wanggezhuang syncline. The area is characterized by three main groups of faults with strikes in the northwest (NW), northeast (NE), and
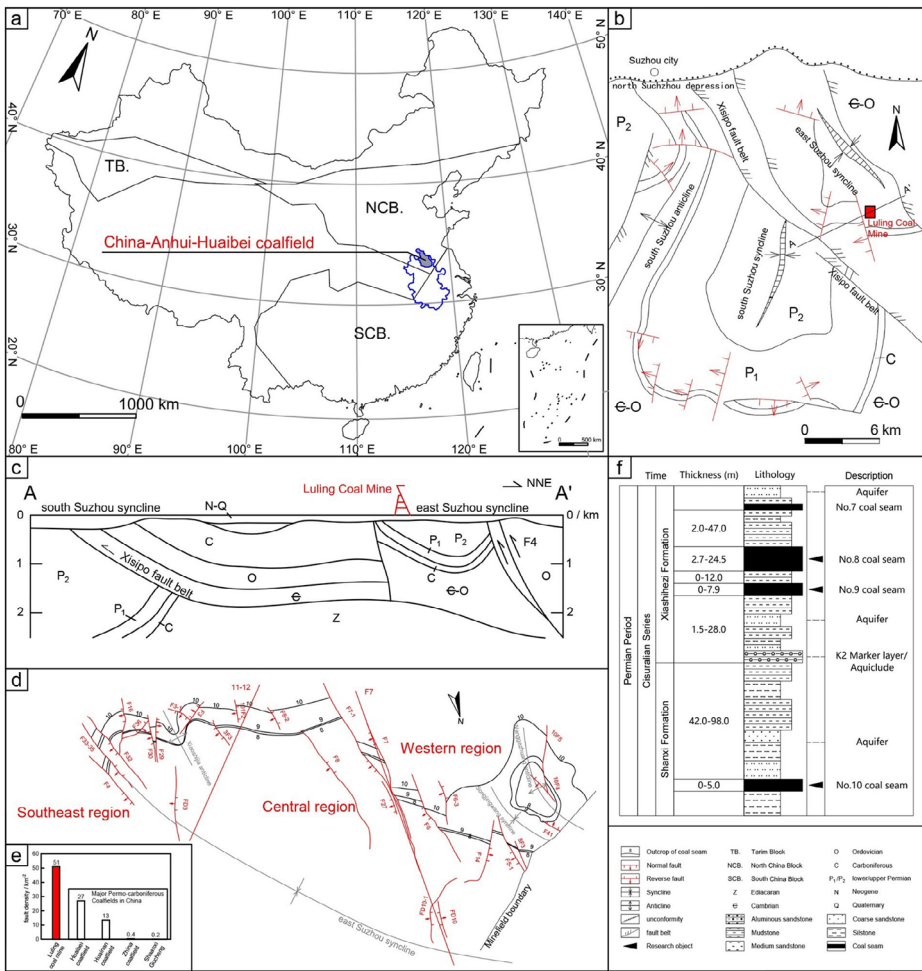
Fig. 1 Geological information of coalbed group in Huaibei coalfield

nearly north-south (NS) directions. The reverse faults predominantly strike in the NS direction and exhibit a vertical displacement ranging from 10 to 50 m. These reverse faults are inclined towards the east and west with a dip angle between 60 and 75 degrees. The normal faults in the area can be classified into two groups based on their strike: NE and NW. These faults dip primarily towards the east and display varying magnitudes of vertical displacement. The maximum drop observed is more than 100 m, while the typical range is between 20 and 50 m. The dip angle of these normal faults ranges from 60 to 80 degrees. The fault plane combination in the area is mainly characterized by a parallel arrangement and "Y" type (Fig. 1(c)). Initially, the faults may exhibit either tensile or compressive properties. However, as time progresses, these mechanical properties undergo torsional transformation to varying degrees.

The minefield is divided into three parts based on the structural features (Fig. 1(c)). The western part, which spans from the minefield boundary to the F7 fault, is primarily affected

by small and medium-sized faults. Within this area, there are 19 faults with a vertical displacement greater than 10 m. The strike of these faults varies significantly, lacking consistent regularity. The main fault in this region trends in a NE direction. The middle part of the minefield, extending from the F7 fault to the 11–12 exploration line, exhibits a relatively simpler structure. It is characterized by the development of seven large and medium-sized faults, predominantly striking in the NE direction. The southeastern part of the minefield, located east of the 11–12 exploration line, is divided into the southeast region. This area is marked by the presence of 13 large and medium-sized faults. The primary strike directions of these faults are NE and nearly NS Additionally, the complex fault relationship in this region is further complicated by the presence of three interlayer faults.

2.2 Vertical distribution of CBM and outburst risk

Based on the analysis of gas pressure and content measurements from the borehole in the Luling coal mine, certain relationships have been established between gas content, pressure, and buried depth (Fig. 2). The Nos. 8 and 9 coal seams are positioned nearly 60 m above the No. 10 coal seam. Based on the general understanding of gas occurrence, it is expected that as the burial depth increases, gas status parameters in deeper coal seams would be higher compared to those in shallower coal seams. However, a statistical analysis of the measured data on gas status parameters in each coal seam reveals a significant difference. Surprisingly, the gradient of gas pressure and content in the Nos. 8 and 9 coal seams is considerably higher than that observed in the No. 10 coal seam. This observation challenges the conventional understanding of gas occurrence and suggests the presence of specific factors influencing the gas behavior in the Luling mine. Further investigation is required to comprehend the underlying mechanisms responsible for this unique gas distribution pattern.

The experimental coal mine has experienced 26 coal and gas outburst accidents, all concentrated in the central part of Nos.8 and 9 coal seams (Fig. 3). The recorded shallowest outburst depth is -298 m, and the most severe observed gas outburst in one incident was 1.23 million cubic meters, with a coal outburst of 10,500 tons. Among them, seven outbursts occurred near geological structural areas, and three outbursts occurred in areas with abrupt changes in coal seam thickness. These regions exhibit characteristics of abnormal ground stress and high gas pressure, making coal and gas outburst accidents highly prone in areas with high gas pressure and structurally complex coal seams. No.10 coal seam, with simple
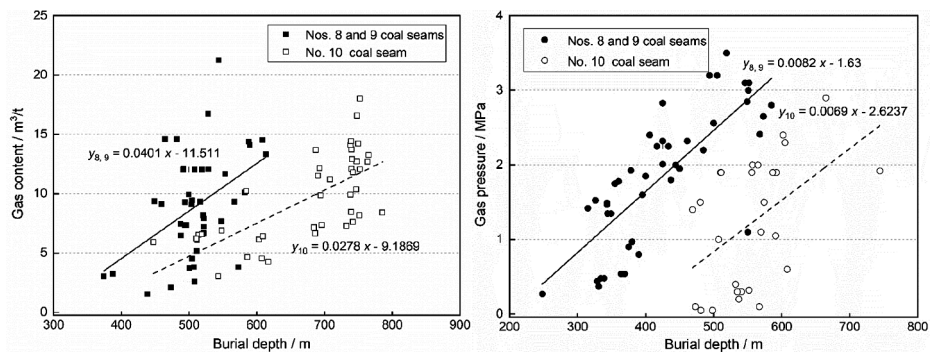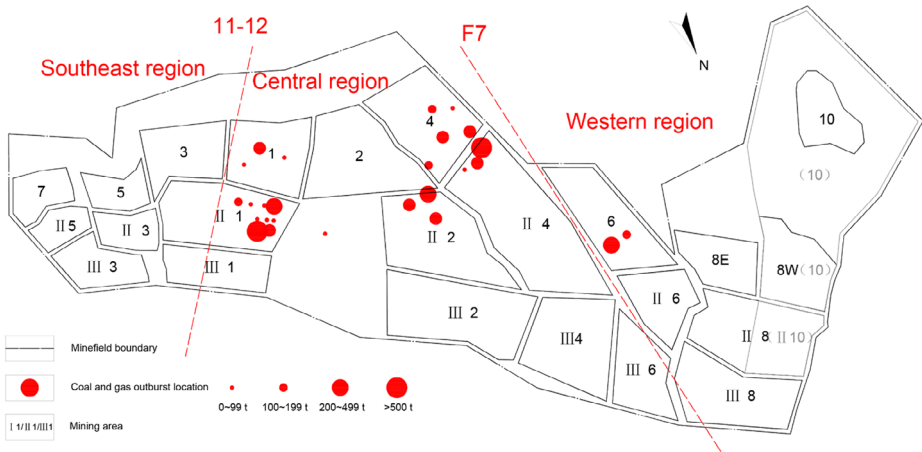

Fig. 2 Variation of gas parameters with depth of burial

Fig. 3 Location and accident scale of coal and gas outburst

geological conditions and lower gas pressure, has not experienced outbursts and is therefore mined as a protective layer for coal seams 8 and 9. The statistical results of accidents reveal a significantly higher risk of coal and gas outbursts in Nos.8 and 9 coal seams compared to No.10 coal seam.

3 Research approach

3.1 Test samples

The samples were taken from the aforementioned Luling coal mine deposits while considering the actual mining conditions. Tectonic coal samples were specifically chosen from the III1 and III2 mining areas, ensuring their comparability for direct comparisons. These freshly exposed coal samples underwent sieving to obtain specific particle sizes necessary for the various tests conducted (Fig. 4).

3.2 Test methods

A comprehensive set of tests was conducted on the coal samples, encompassing various analyses such as particle size distribution, carbon isotope analysis, proximate analysis, infrared spectrum analysis, SEM analysis, methane adsorption analysis, and low-pressure nitrogen adsorption/desorption analysis (Table 1).

Coal's carbon isotope was determined using Gas Stable Isotope Mass Spectrometer (MAT253-EA, Thermo Fisher Scientific). Results were expressed as delta (δ) values relative to VPDB standard (Ding et al. 2019):

$$\delta^{13}C(\%) = \left[\frac{R\left(^{13}C/^{12}C_{\text{sample}}\right)}{R\left(^{13}C/^{12}C_{VPDB}\right)} - 1 \right] \times 1000$$
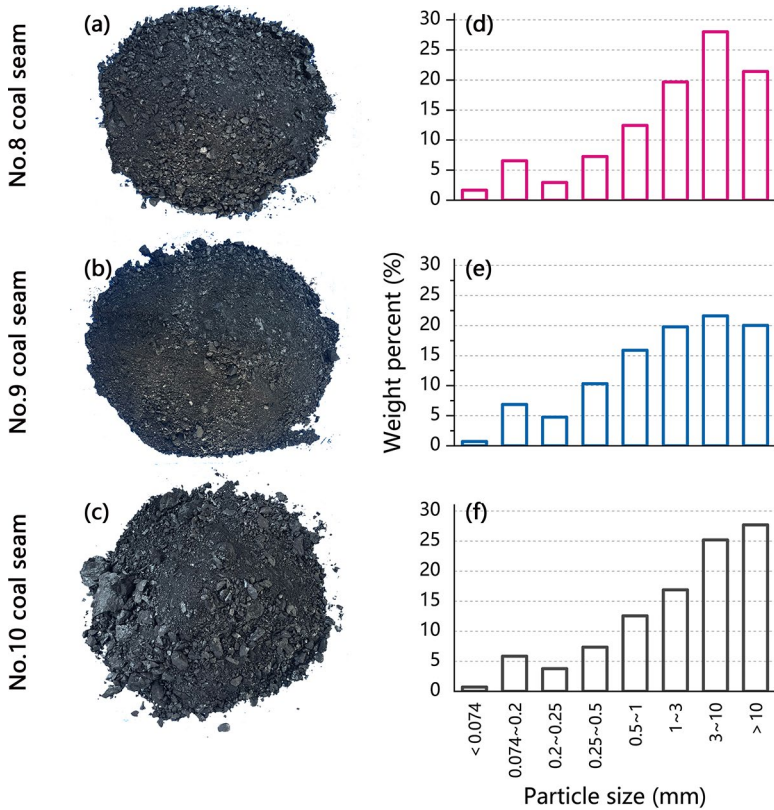
Fig. 4 Coal samples and particle size distribution

where, $R\left({}^{13}C/{}^{12}C_{VPDB}\right)$ is the carbon isotope abundance ratio of VPDB.

Analysis of coal samples using automatic analyzers to obtain the proportion of moisture, ash and volatile matter, etc. in coal samples, according to the Chinese national standard GB/T212-2008.

The NCOLET 6700 in situ test system was employed for Fourier transform infrared spectroscopy analysis of the coal samples. Infrared spectrograms were generated by analyzing the reflected light, which arises from the distinct surface structures of the samples. By studying the characteristic wave numbers reflected by different chemical structures, the type of substance and main functional groups present in the samples could be identified.

To determine the particle size distribution (PSD) of structurally smaller coals (<1 mm), the Bettersize-2600 Laser Particle size analyzer was utilized. Each coal sample below the 1 mm threshold, following screening, was selected for this test. The coal samples were subjected to ultrasonic dispersion for 10 min, after which the volume distribution of particle groups could be automatically outputted.

The HITACHI S-3000 N scanning electron microscope (SEM) was employed to observe the micron cracks and micropores on the surface of coal particles. To ensure accurate observations, a relatively flat natural section was selected as the observation surface.

Table 1 Influencing factors and test methods

Influencing factor	Research objective	Test method	Particle size (mm)	The influence on gas
Intrinsic factors	Thermal maturity	Proximate analysis	0.074-0.2	Generation
	Molecular structure	FTIR	<0.074	Storage
	Pore structure	N_2 adsorption/ SEM	Full particle size	Storage
	Adsorption characteristics	CH_4 adsorption	Full particle size	Storage
Extrinsic factors	Coal forming conditions	Carbon isotope	<0.074	Generation
	Particle size distribute	Better-size-2600/ Sieves	Full particle size	Storage
	Coal seam thickness	—	—	Generation、Storage
	Tectonic coal distribution	—	—	Storage
	The lithology of roof and floor	—	—	Storage
	Aquifer distribution	—	—	Storage
	Tectonic history	—	—	Generation、Storage

Full particle size 0.074-0.2, 0.2–0.25, 0.25–0.5, 0.5–0.1, 1–3

The pore structure characteristics of coal samples with different crushing degree were analyzed and determined using the AUTOSORB-iQ2 automatic liquid nitrogen analyzer. The experiment followed international standards, maintaining a liquid nitrogen temperature of 77 K throughout the test. The aperture measurement range for this analysis was set between 0.35 and 500 nm.

The adsorption capacity of samples under varied gas pressure conditions was determined using the HCA high-pressure capacity methane adsorption device. The test gas used was CH_4, and the temperature was set at 30 °C.

4 Results

## 4.1 Carbon isotope and proximate analysis

The results of the Carbon isotope analysis indicate that there is no significant difference in the carbon isotope values among the different coal seams, with values ranging between

Table 2 Test results of carbon isotope ratio of each coal seam

Samples	$\delta^{13}C/\%$	$M_{ad}/\%$	$A_{ad}/\%$	$V_{ad}/\%$	$FC_{ad}/\%$	$A_d/\%$	$V_d/\%$	$V_{daf}/\%$	$FC_d/\%$
8−1	−24.24	1.65	27.25	32.48	38.62	27.70	33.03	45.68	39.27
8−2	−24.09	1.63	22.31	32.37	40.69	25.68	32.91	42.56	41.41
9−1	−24.24	1.91	29.59	27.67	40.83	30.17	28.21	40.39	41.62
9−2	−24.29	1.92	31.62	27.81	38.65	32.24	28.36	41.85	39.40
10−1	−23.91	1.76	27.30	27.88	43.06	27.79	28.38	39.30	43.83
10−2	−24.03	1.78	26.41	27.66	44.15	26.89	28.16	38.52	44.95
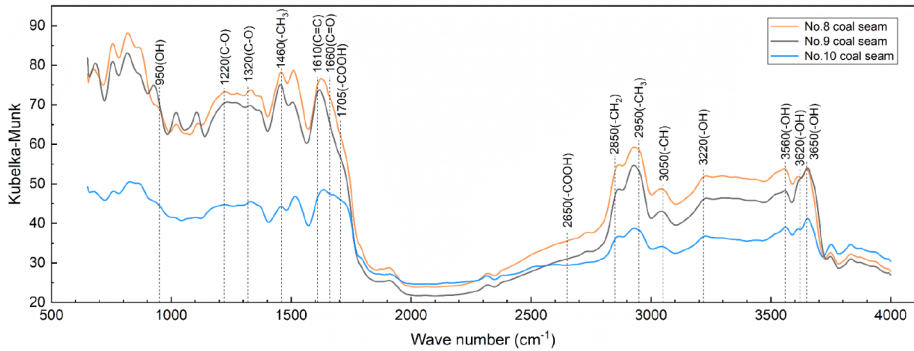
Fig. 5 FTIR test spectrum of coal samples

-23.91 and -24.29% (Table 2). These values suggest that all three coal seams are composed of C3 plants, which is consistent with the composition of coal seams deposited during the Carboniferous Permian period (Suto and Kawashima 2016). The ash content (A_{ad}) in coal tends to increase with higher mineral content, which can have an adverse effect on methane adsorption within the coal seam. In this study, the ash of the No. 8 coal seam is the lowest, averaging at 24.78%. This lower ash content indicates that the No. 8 coal seam is more beneficial for gas storage compared to the other coal seams. As the coalification degree increases, the volatile matter content (V_{daf}) in coal tends to decrease (Cheng et al. 2021). The data obtained suggest that the coalification degree of the deep coal seam is higher than that of other coal seams. This indicates that the amount of gas produced per unit volume of No. 10 coal is larger compared to the No. 8 and No. 9 coal seams.

4.2 Functional groups in coals

The results of the standard FTIR spectra of the three samples are shown in Fig. 5. The observed trends in the abundances of functional groups in these samples were consistent with previous findings, indicating a gradual decrease in abundance with increasing coalification (Chen et al. 2012). The Lambert-Beer law states that the concentration of functional groups is directly proportional to the absorbance of light, which can also be expressed in terms of the Kubelka-Munk function. This principle allows for the quantitative analysis of each active group present in the coal samples (Cai et al. 2019; Wang et al. 2017).

Given the diverse, complex, and heterogeneous nature of coal structures, the absorption summits of functional groups often exhibit multi-peak superposition. Directly obtaining the

amount of superposition from the spectral line is not feasible. Thus, it becomes necessary to fit the absorption peaks associated with the characteristic groups present in coal samples. To achieve this, a segmented processing approach can be employed using a wave number of 2000 cm^{-1} as a node. This involves selecting an appropriate half peak width and fitting the two sections of the spectrum separately. Through this process, the position, height, and content of each peak can be determined, providing valuable insights into the composition of the samples (Fig. 6).

4.3 Coal sample particle size

The PSDs of the samples can be observed in Fig. 4. The distribution, obtained using the screening method, indicates that the No. 10 coal seam contains a larger proportion of large coal particles (>10 mm). In contrast, the No. 8 coal seam predominantly consists of smaller
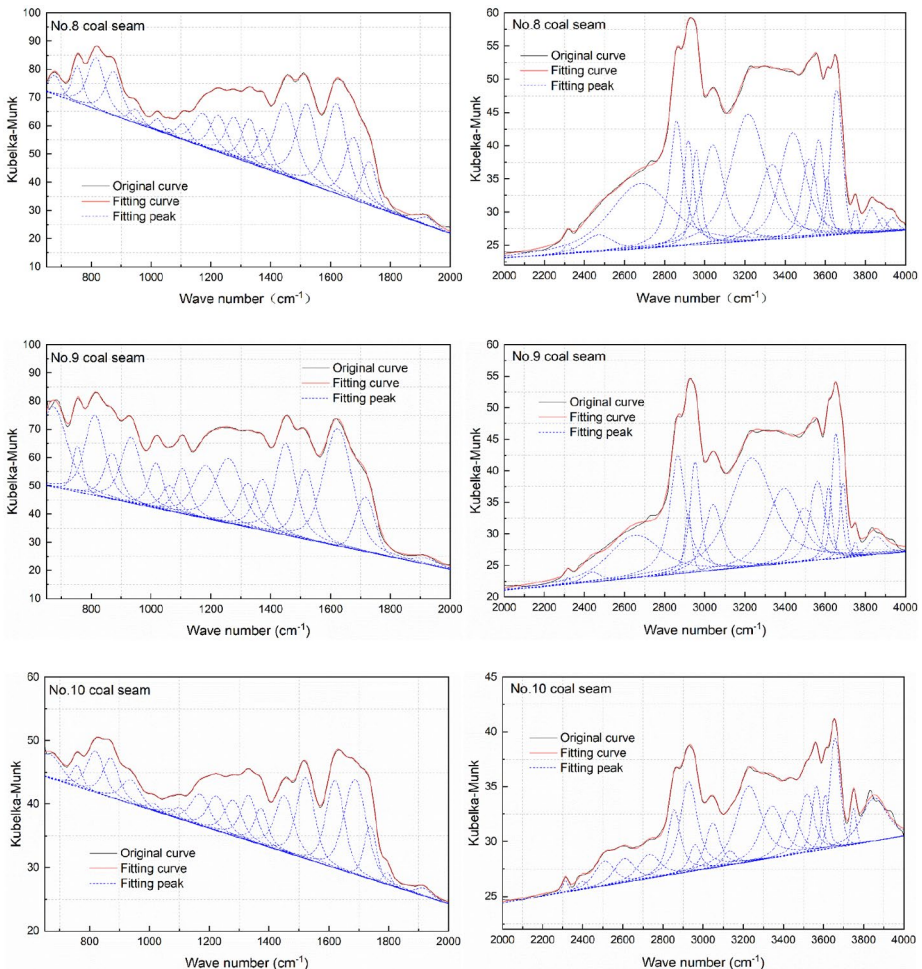

Fig. 6 Peak fitting diagram

coal particles (<0.074 mm). The No. 9 coal seam shows a higher concentration of particles within the range of 0.074–10 mm.Based on these findings, the PSD within the range of 0–0.5 mm, determined using a laser particle size tester, is presented in Fig. 7(a-c). For the No. 8 coal seam, a distinct bimodal distribution is observed, with peaks at 50 μm and 200 μm, respectively. Conversely, the No. 9 coal seam exhibits a characteristic single-modal distribution, with a peak at 105 μm. The No. 10 coal seam displays a relatively insignificant bimodal distribution.

4.4 Methane sorption capacities

The Adsorption isotherm for methane of the samples can be observed in Fig. 8. The range of methane adsorption capacity for each coal seam sample under the maximum pressure is reported as 26.89–34.61 ml/g, 26.23–34.24 ml/g, and 12.09–14.53 ml/g, as indicated in Fig. 8. Comparing the samples within the same coal seam, it is evident that the adsorption limit of methane increases with both an increase in gas pressure and a decrease in sample particle size (Table 3). This relationship suggests that higher gas pressures and finer particle sizes contribute to greater methane adsorption. Furthermore, when comparing the methane adsorption capacities among the different coal seam samples, it is noteworthy that the Nos. 8 and 9 coal seams demonstrate significantly higher methane adsorption capacities compared to the No. 10 coal seam.
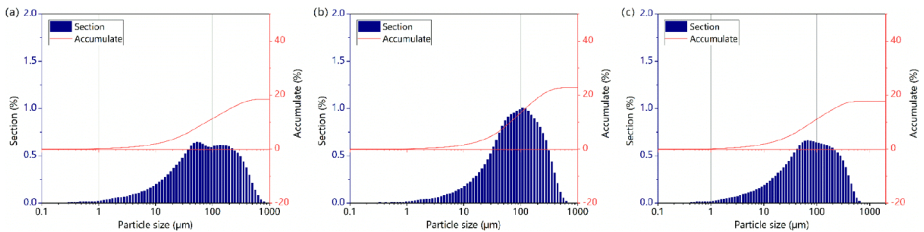

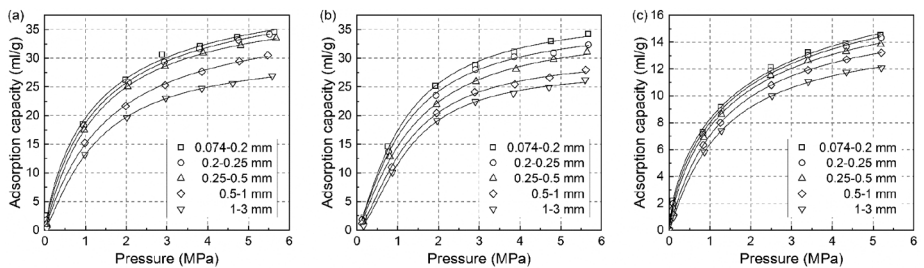**Fig. 7** Particle size distribution of coal samples

Fig. 8 Isothermal adsorption curve of coal samples

Table 3 Adsorption constants for samples with different intervals of particle size

Samples	Size(mm)	VL(m^3/t)	PL^{-1} (MPa^{-1})	R^2
No. 8 coal seam	1–3	31.11	0.7399	0.9964
	0.5-1	38.34	0.6473	0.9992
	0.25–0.5	40.26	0.7874	0.9992
	0.2–0.25	43.09	0.7690	0.9999
	0.074-0.2	44.07	0.8020	0.9983
No. 9 coal seam	1–3	28.03	0.7022	0.9992
	0.5-1	30.49	0.7343	0.9991
	0.25–0.5	35.47	0.7043	0.9987
	0.2–0.25	36.61	0.8104	0.9993
	0.074-0.2	38.26	0.8354	0.9986
No. 10 coal seam	1–3	14.84	0.7622	0.9998
	0.5-1	16.67	0.7358	0.9975
	0.25–0.5	18.92	0.6868	0.9992
	0.2–0.25	20.61	0.6380	0.9990
	0.074-0.2	22.05	0.6012	0.9981

4.5 Nitrogen adsorption and desorption

The adsorption curves of the tested samples exhibit a characteristic half-U shape, resembling the shape of a golf club. These coal adsorption isotherms were compared with the IUPAC classification (Thommes et al. 2015). According to the classification, the coal adsorption isotherms fall into the category combining features of both Type II and Type IV curves, indicating that coal can be considered a type of porous adsorbent. As the relative pressure increases, the desorption curve and adsorption curve gradually separate from each other, eventually closing after the formation of a distinct hysteresis loop in the intermediate pressure range (as shown in Figs. 9, 10 and 11). This hysteresis phenomenon suggests the presence of pore structures within the coal samples that result in variations in adsorption and desorption behavior.

Comparing the adsorption isotherms of samples with different particle sizes, it is noticed that the sample's adsorption rate and adsorption capacity increase gradually as the particle size decreases. This indicates that finer particle sizes lead to an increase in both the rate and capacity of adsorption. The maximum nitrogen (N_2) adsorption capacities for the three groups of coal samples are reported as 1.76, 2.21, and 2.15 m^3/g, respectively. These values represent the maximum amount of N_2 that can be adsorbed per unit mass of the coal samples.

Microscopic analysis of the three coal seam samples revealed the presence of micron-sized surface pores and fissures. Different magnifications were used to observe these features in detail.

At high-power magnification (Fig. 12), the developed primary fractures were clearly visible. These fractures appeared to be well-sealed, with a significant amount of fine slag attached around them. Additionally, mineral particles were observed to fill the fractures, indicating their presence within the coal sample.

Under low-power magnification (Fig. 13(a)), the surface of the coal samples appeared relatively flat, but numerous fractures were observed. Upon closer inspection using high-power magnification (Fig. 13(b)), the primary fractures were seen to be distributed in a den-
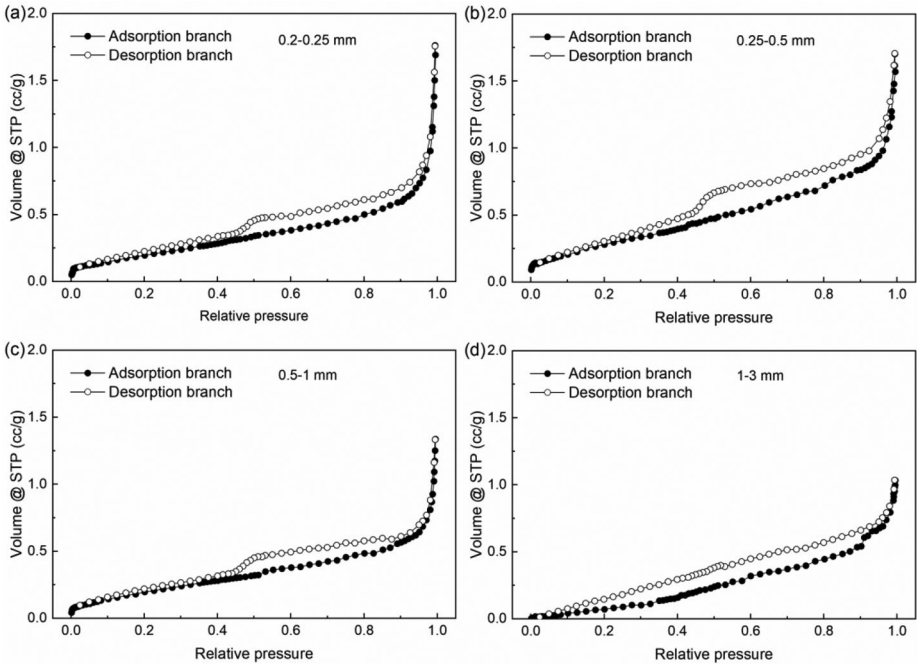
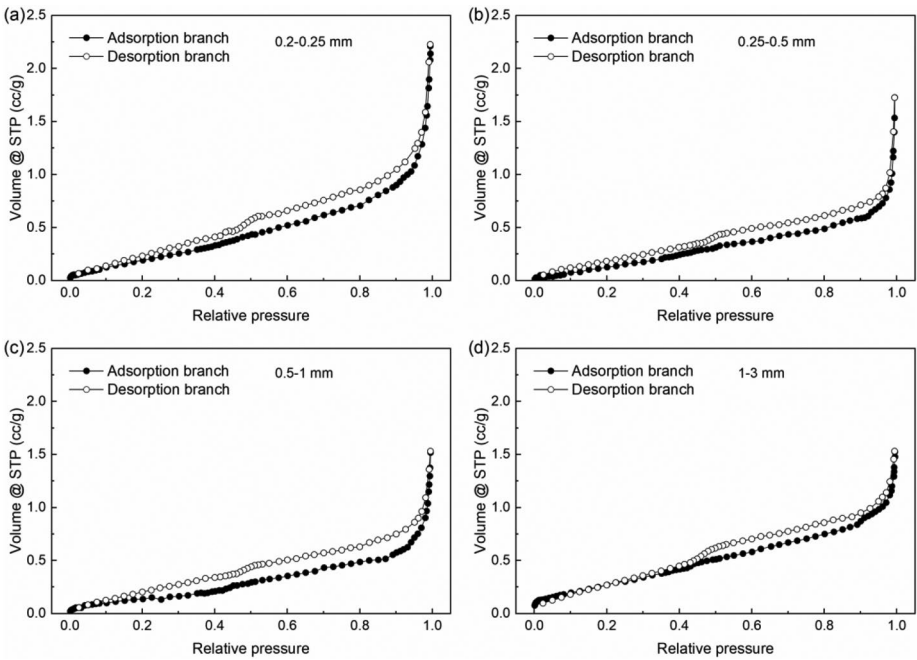**Fig. 9** N_2 adsorption/desorption curve of the No.8 coal seam samples

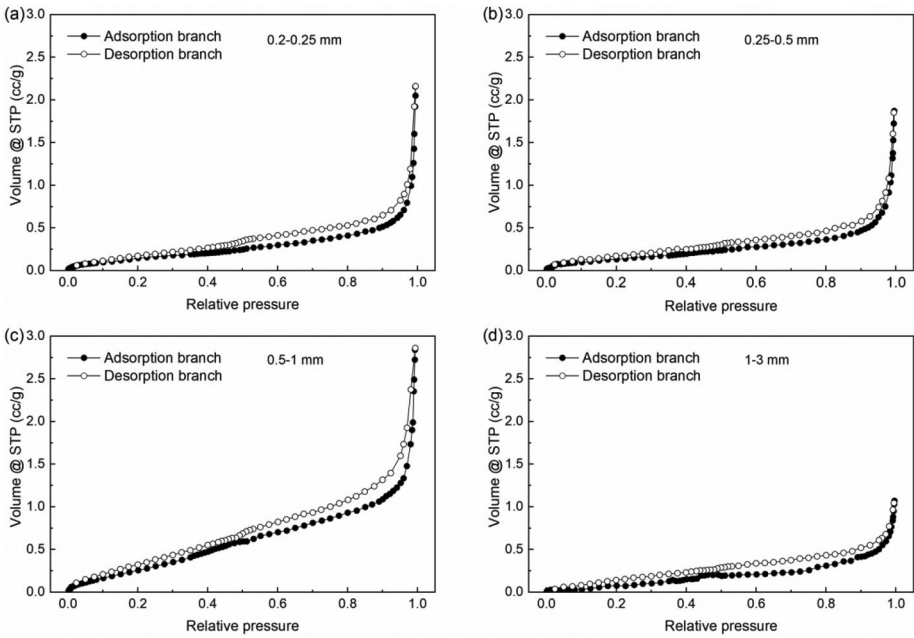**Fig. 10** N_2 adsorption/desorption curve of the No.9 coal seam samples

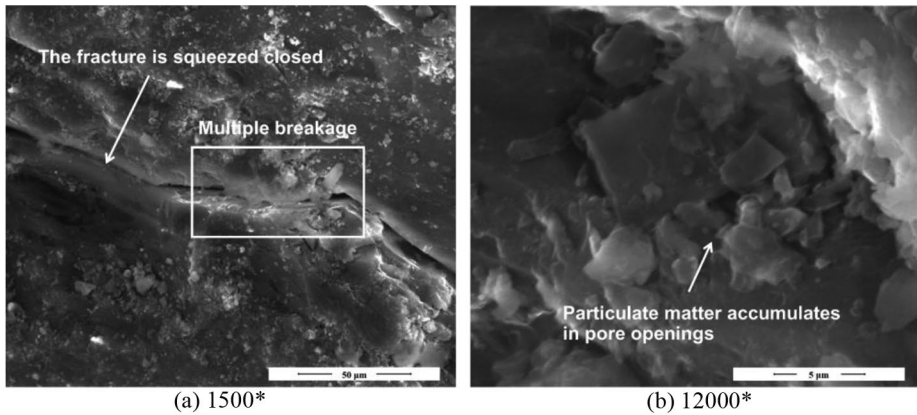**Fig. 11** N$_2$ adsorption/desorption curve of the No. 10 coal seam samples

Fig. 12 SEM pictures of samples from the No. 8 coal seam

dritic pattern. Some fine slag was attached around these fractures, and there was evidence of partial blockage in certain areas.

Further examination using high-power magnification (Fig. 14) revealed well-developed primary fractures characterized by their smooth surfaces. Thick slag deposits were also apparent, and blockage phenomena within the fractures were observed. However, despite these blockages, the fractures displayed good openness.
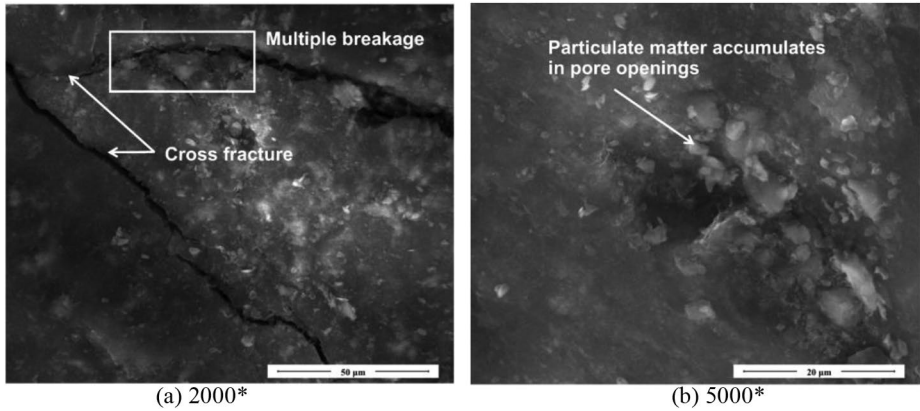
(a) 2000*   (b) 5000*

Fig. 13 SEM pictures of samples from the No. 9 coal seam

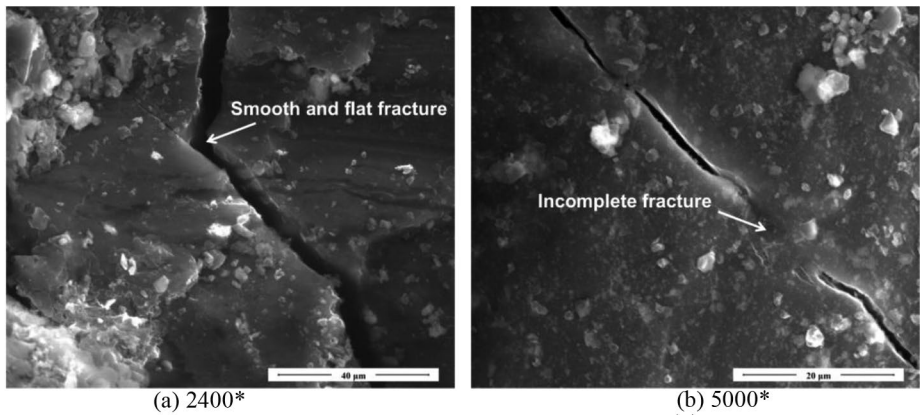(a) 2400*   (b) 5000*

Fig. 14 SEM pictures of samples from the No. 10 coal seam

Comparing the electron microscope scans of coal samples, it was evident that each sample exhibited varying degrees of pore and fissure development. The coal samples from the Nos. 8 and 9 seams exhibited mineral particle accumulation within their fissures, which were characterized by small crack ports and limited openness. In contrast, the No. 10 coal seam displayed pronounced fracture development, featuring large fractures with good transparency.

5 Discussion

5.1 Effect of coal seam burial and tectonic history on CBM occurrence

The No. 10 coal seam (SQ3) originated within a tidal flat and lagoon sedimentary system (Fig. 15(a)), while the Nos. 8 and 9 coal seams (SQ4) formed within a deltaic sedimentary
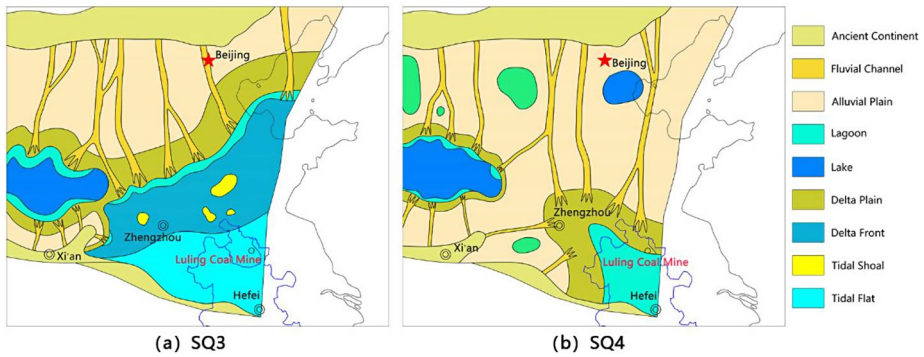
Fig. 15 Lithofacies paleogeography map of SQ3 and SQ4 in the North China Basin
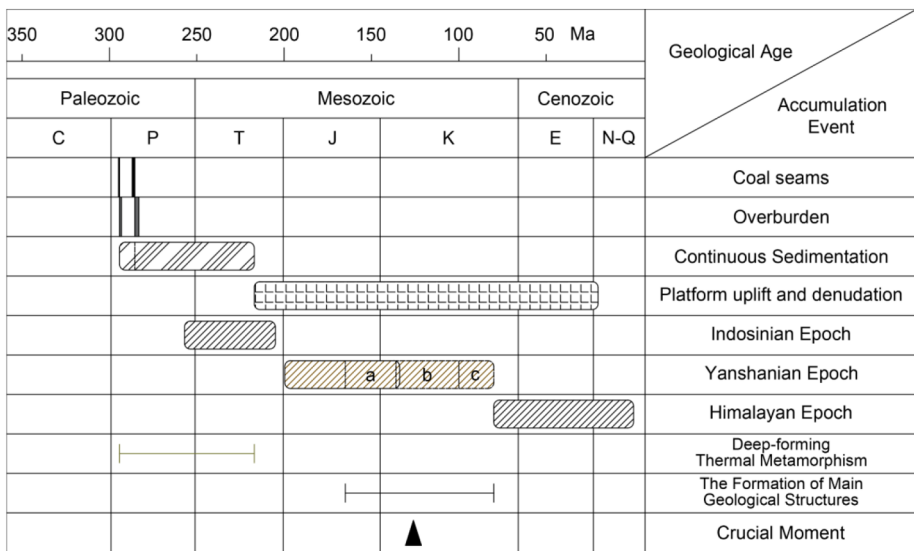

Fig. 16 Gas system reservoir forming event map

system (Fig. 15(b)) (Li et al. 2021; Shao et al. 2014). The deltaic depositional system is primarily influenced by fluvial processes, providing a stable sedimentary environment with ample terrigenous input, facilitating the development of thick coal seams. In contrast, the tidal flat and lagoon depositional system is characterized by tidal action, where the sedimentary environment is influenced by fluctuations in sea level and basin subsidence rates (James R. Staub, Arthur D. Cohen, 1979). This results in an unstable sediment supply, leading to relatively thin coal seams in this depositional environment.

Following the platform stabilization period from the Permian to the early Triassic, the North China Basin experienced continuous subsidence of the strata and the occurrence of hypogenic thermal metamorphism within the coal seams (Fig. 16). However, the Late Indosinian movement disrupted the stable sedimentary process during the early stage. As a result, the entire platform underwent uplift, leading to denudation of the original sedimen-

tary strata, including the absence of Triassic and part of Permian strata. After the Indosinian movement, the North China platform entered the Yanshan movement period, which was a significant moment in the formation of the main structures in the Luling coalfield. This period can be classified into three distinct stages:

a) Strong Compression Stage: During this stage, synclinal structures and thrust faults developed within the coalfield.

b) Main Extension Stage: In this stage, normal faults were formed, and some reverse faults underwent a transformation into normal faults within the coalfield.

c) Weak Compression Stage: This stage was characterized by the presence of a few thrust faults within the coalfield.

Furthermore, influenced by the Himalayan movement, the strata descended as a whole and were subsequently covered by Cenozoic sediments, eventually forming the present-day coal measure strata system.

Through a comparative analysis of the coal seam accumulation process, it becomes evident that the geological structures of the three coal seams are fundamentally similar because they have been subjected to the same tectonic action. Consequently, the variation in gas content among these seams can be attributed to factors other than large-scale tectonic forces. However, it is important to highlight that differences in sedimentary environments have played a crucial role in shaping variations in lithology and coal thickness. These differences have subsequently influenced the degree of coalification and the resulting gas content within the seams.

In summary, while the geological structures of the three coal seams are similar due to experiencing the same tectonic action, it is the divergent sedimentary environments that have exerted the most significant influence on the variations in lithology, coal thickness, and ultimately the gas content of these seams.

5.2 Effect of coal seam occurrence environment on CBM occurrence

The sealing effect of gas is directly influenced by the lithology of the roof rock. Based on the information provided in Table 1, the roof of No. 8 coal seam consists primarily of mudstone, while the roof of No. 10 coal seam is mainly composed of medium-grained sandstone. The permeability of rock varies depending on its lithology, with sandstone having higher permeability, followed by coal, and then mudstone (Sandstone permeability > coal permeability >> mudstone permeability)(Guo et al. 2021a; Karacan and Goodman 2012). This discrepancy in permeability results in different sealing effects for the two coal seams. Therefore, the No. 8 coal seam exhibits a good sealing effect primarily due to the presence of a thick mudstone roof, which forms a natural dense cap. This cap effectively prevents the evaporative escape of gas from the seam, enhancing its potential for gas retention.

Furthermore, the coal seam serves as both the source and reservoir of gas. The thickness of the coal seam directly influences the volume of gas generated. Generally, in areas with good sealing effects, the thickened coal seam tends to be the areas of gas enrichment. This is because the enhanced sealing prevents the escape of gas, allowing it to accumulate and increase in concentration within the thicker portions of the seam.

To summarize, the sealing effect of gas is closely linked to the roof lithology. The No. 8 coal seam benefits from a strong sealing effect due to the substantial mudstone roof, which restricts the evaporation of gas. Additionally, as the thickness of a coal seam enlarges, so

does the potential for gas generation and storage. In regions with favorable sealing conditions, the thicker zones within the coal seam are typically associated with higher gas enrichment.

5.3 Effect of functional groups in coal on gas occurrence

The results indicate that the functional groups in coal has significant effects on both methane production and storage in coalbeds. In terms of production, as the level of metamorphism increases, the content of aliphatic hydrocarbons gradually decreases while methane production increases (Sun et al. 2022). This suggests that higher metamorphism levels enhance the production of methane.

On the other hand, when considering methane storage, the presence of hydrophilic oxygen-containing functional groups in coal has an inhibitory effect on methane adsorption (Fu et al. 2023, 2024). As the proportion of these oxygen-containing functional groups increases, the adsorption capacity of coal for gas decreases. This means that the coal becomes less capable of storing methane.

Comparing different coal seams, the No. 10 coal seam exhibits lower methane adsorption capacity compared to other seams. This might be attributed to the fact that the No. 10 coal seam has the highest proportion of oxygen-containing functional groups. Although it has the highest production of methane per unit volume (as shown in Table 4), its lower methane adsorption capacity limits its storage potential.

5.4 Effect of pore characteristics on CBM occurrence

Regarding pore morphology, all three coal samples exhibit H4-type hysteresis rings. However, the hysteresis rings in the No. 10 coal seam are less pronounced, suggesting the presence of closed cylindrical pores with poor connectivity at one end. On the other hand, Nos. 8 and 9 coal seams primarily exhibit flat, through-pores with obvious hysteresis rings formed by elongated pores. This observation suggests that Nos. 8 and 9 coal seams have undergone more substantial restructuring compared to the No. 10 coal seam.

Gas primarily adsorbs onto the surfaces of micropores and mesopores within coal. Therefore, the volume of micropores directly influences the storage capacity of gas. In the case of the investigated coal seams, the micropore volume of Nos. 8 and 9 is noticeably higher than that of No. 10 (Fig. 17). Consequently, the adsorption methane capacity of Nos. 8 and

Table 4 Peak area and proportion of main functional groups of coal samples in each coal seam

| Functional group		No. 8 coal seam		No. 9 coal seam		No. 10 coal seam	
		Peak area	Proportion	Peak area	Proportion	Peak area	Proportion
Aliphatic hydrocarbon	-CH$_3$/-CH$_2$-	8905.0	24.2%	8865.9	23.4%	3365.9	22.4%
	-CH	2809.4		1594.6		466.5	
Aromatic hydrocarbon	C=C	6705.1	13.9%	6476.6	14.4%	2321.5	13.6%
Oxygenated groups	-OH	16031.6	61.9%	15688.3	62.3%	5275.3	64.0%
	C=O	2018.4		1670.1		1660.2	
	COOH	5407.8		3094.7		1147.5	
	C-O	5497.3		6611.0		2455.2	
	COO-	926.3		877.9		413.8	
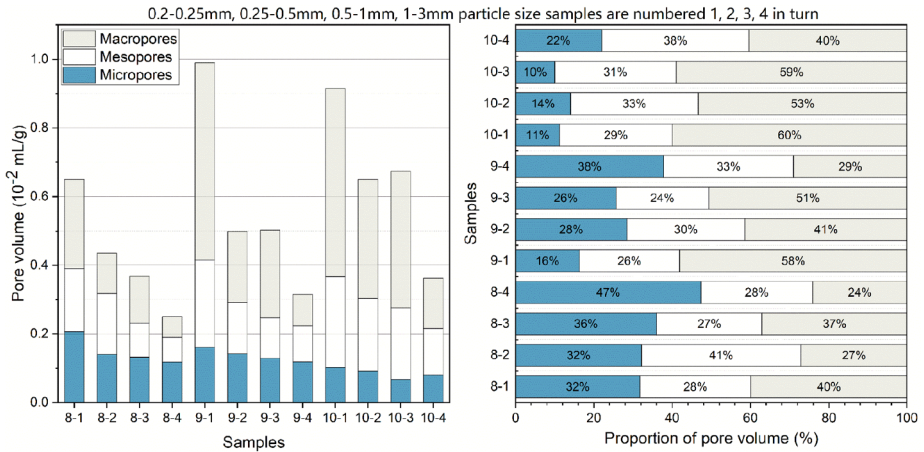
Fig. 17 Experimental results of pore volume

9 coal seams exceeds that of the No. 10 coal seam. The incremental increase in the limit gas adsorption capacity for samples with sample sizes of 1–3 mm and 0.074–0.2 mm in Nos. 8, 9, and 10 coal seams is 12.96, 10.23, and 7.21 m^3/t, respectively. This implies that as the coal fragmentation degree increases, the methane adsorption capacity experiences a significant enhancement, particularly for coal seams characterized by a larger proportion of micropores. Therefore, these findings demonstrate the importance of micropore volume in determining the adsorption methane capacity of coal seams. Higher micropore volumes imply a greater potential for coal seam gas storage.

Upon comparing the scanning electron microscope results of coal samples, it is evident that all samples exhibit varying degrees of pore fracture development. In the case of Nos. 8 and 9 coal samples, the fractures are visibly pronounced and exhibit a rough surface texture. Additionally, there is an accumulation of mineral particles within the fractures, resulting in small fracture openings with limited connectivity. Conversely, the No. 10 coal seam displays significant fracture development characterized by smooth and complete fractures with larger openings, indicating better connectivity within the coal structure. Combined with the pore characteristics, it can be seen that Nos. 8 and 9 coal seams have better storage limits and poor fracture connectivity, which is not suitable for gas escape, while No. 10 coal seams have poor storage capacity and good fracture connectivity, which is not conducive to gas enrichment.

5.5 Effect of tectonic coal characteristics on gas occurrence

5.5.1 Regional distribution of tectonic coals

The No. 8 coal seam exhibits a tectonic coal thickness ranging from approximately 65–90%. In the southeastern region of the mine field, the tectonic coal thickness accounts for 75–80% of the total coal seam thickness. The middle section of the coal seam experiences the most significant development of tectonic coal, constituting over 95% of the entire bed. This condition is particularly prominent in the 4 and II 4 mining areas, where almost the entire

coal seam consists of tectonic coal. In the western structure, the tectonic coal accounts for 65–70% of the total thickness.

The No. 9 coal seam has only a few intact coal seams visible in the exposed area, with the gtining portion being tectonic coal. The thickness of tectonic coal in this seam exceeds 20% of the total coal seam thickness. In the case of the No. 10 coal seam, the tectonic coal is powdery in nature and stably distributed under the roof with a thickness ranging from 0.15 to 0.3 m.

Although all three coal seams underwent the same geological tectonic period, the distribution of regional geological structure and tectonic coal is not entirely consistent. The presence of tectonic coal is primarily influenced by small faults and the seam thickness. Analysis of exploration data and exposed faults in the mined areas reveals that small structures predominantly consist of faults smaller than the thickness of the coal seam. In the No. 8 coal seam, the faults mainly manifest as sliding faults along the coal seam. This occurrence can be attributed to the principle of interzonal slip, which tends to occur in lower-strength rock layers. As the coal seam belongs to a relatively soft stratum, especially when it is thick, horizontal tectonic stress easily induces sliding friction, resulting in the formation of tectonic coal. Subsequently, under the influence of multi-stage tectonic movements, the consolidated tectonic coal is gradually destroyed, leading to an increase in the thickness of tectonic coal over time.

5.5.2 Tectonic coal particle size distribution

Based on the sieving method and PSD analysis of the tectonic coal, it has been observed that the No. 10 coal seam exhibits the lowest degree of failure, with a significant presence of large samples. In contrast, the No. 8 coal seam contains a higher proportion of extremely fine particles compared to the No. 9 and No. 10 coal seams. The No. 9 coal seam demonstrates a relatively even breakdown, with small particles comprising the largest proportion. During the laser particle size testing of the 0.5–1 mm sample from the No. 8 coal seam, a noticeable disintegration phenomenon was observed (Fig. 18). This resulted in a sudden increase in the shading rate, making it difficult to accurately determine the particle size distribution in that particular range. This indicates that the tectonic coal sample from the No. 8 coal seam exhibits distinct characteristics of reconstitution.
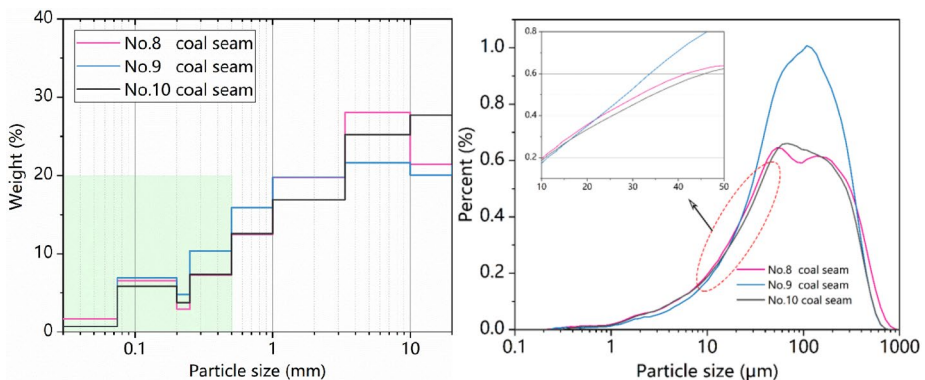
Fig. 18 Particle size distribution of 0–0.5 mm coal samples

Combining the findings from mechanical screening and laser particle size testing, it was observed that in the 0–0.5 mm interval, the No. 8 coal seam has the highest proportion of particles smaller than 50 microns, while the No. 9 coal seam exhibits the highest overall proportion. This suggests that the Nos. 8 and. 9 coal seams have experienced a greater degree of tectonic activity compared to the No. 10 coal seam. Methane adsorption and pore volume tests show that the methane adsorption limit increases gradually with decreasing particle size. Therefore, the occurrence of gas in the Nos. 8 and 9 coal seams is better than in the No. 10 coal seam. This is likely due to the more extensive distribution of tectonic coal and the presence of more fractured tectonic coal in the Nos. 8 and 9 coal seams.

5.5.3 Calculation of methane adsorption capacity of tectonic coal

The Langmuir volume of methane is a crucial parameter for estimating gas reserves. However, the standard testing method only provides methane capacity measurements for granular coal within the 0.2–0.25 mm sample size range, leading to significant errors in estimating coal gas content. To address this issue, the methane adsorption capacity of tectonic coal (considering particle size distribution), denoted as VL_T, is utilized to evaluate the gas content.

$$VL_T = \sum_{i=1}^{n} VL_i w_i$$

where VL_i represents the Langmuir volume at different particle sizes, and w_i denotes the mass percentage of different particle grades. By considering these parameters, the calculated methane limit adsorption capacities for the three coal seams are 37.00, 32.04, and 17.43 m^3/t. The results demonstrate that the maximum gas storage capacity of the No. 8 coal seam is 2.12 times as large as that of the No. 10 coal seam. This method enables more accurate estimation of the coal seam storage capacity in the specified area.

5.6 The evolution process of adjacent coal seams and CBM

During the initial stage of formation, each coal seam underwent distinct sedimentary processes. The thicker Nos. 8 and 9 coal seams were formed due to significant terrigenous replenishment, while the thinner No. 10 coal seam experienced less terrigenous input. Additionally, variations in sedimentary environments resulted in differences in the roof and floor lithology of each coal seam. The mudstone roof of the Nos. 8 and 9 coal seams exhibited better sealing effects compared to the No. 10 coal seam. Following a prolonged period of plutonic metamorphism, the No. 10 coal seam underwent extensive metamorphic changes, generating a considerable amount of gas (Fig. 19(e-f)).

Subsequently, the strata experienced three phases of tectonic activity, which played a crucial role in the significant differences in vertical gas occurrence in the test coal mine. Firstly, there was a stage of strong extrusion, where the soft nature of the coal seam relative to surrounding rocks resulted in the formation of sliding fractures and deformations along the coal seam (Fig. 19(a-b)). During this stage, the thick coal seams (Nos. 8 and 9) underwent significant structural transformations, creating numerous coal body structures and generating a large number of pores that served as larger containers for coal seam gas. The No. 10 coal
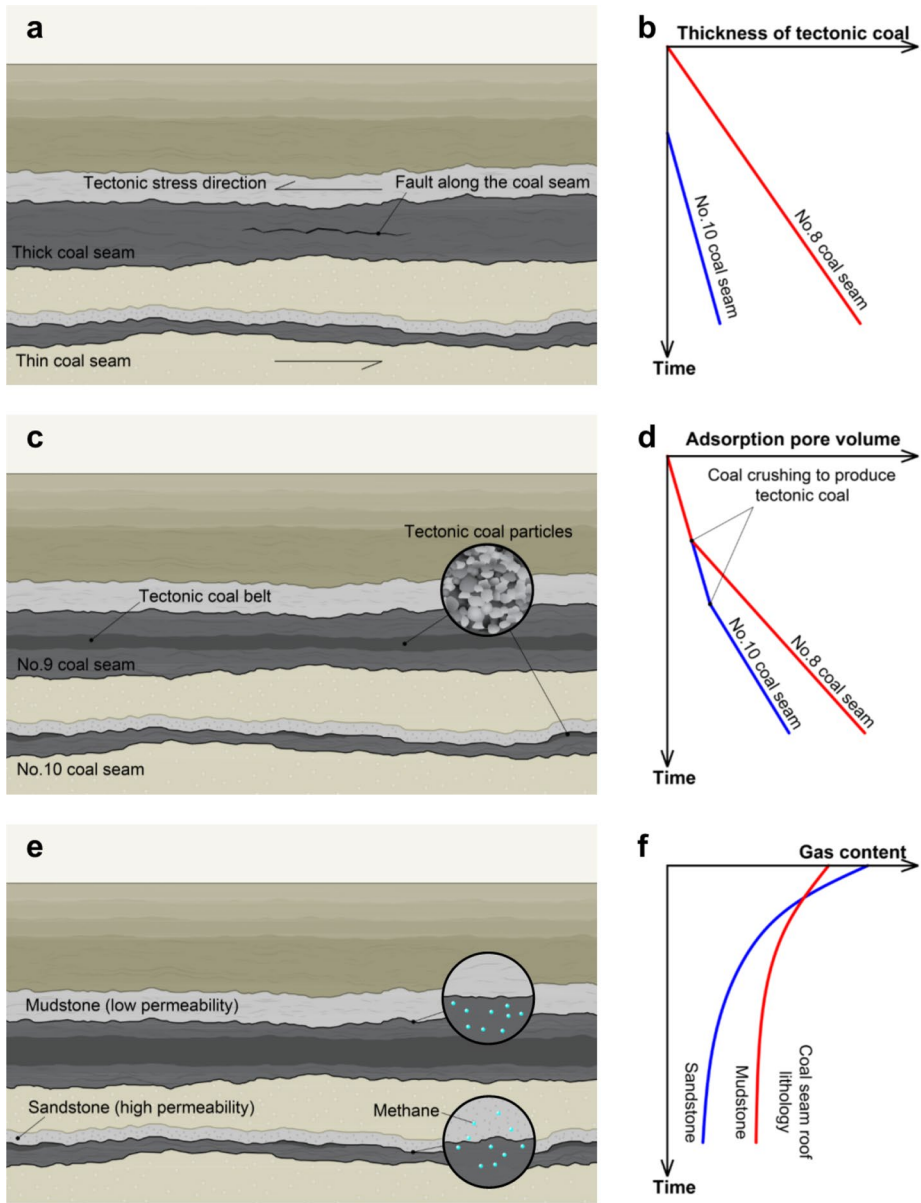
Fig. 19 Evolution process of coal seam and gas

seam underwent relatively limited transformation, with smaller structures mainly forming in the coal seam and its immediate roof (Fig. 19(c-d)). Afterward, the strata entered the main extension stage, during which numerous open normal faults formed, leading to the escape of a significant amount of gas from each coal seam. In the subsequent weak extrusion stage, further damage and restructuring of the coal seam occurred. Only through this complex evolutionary process did the current gas occurrence characteristics of the Luling coal mine emerge.

5.7 Effect of gas occurrence characteristics on coal and gas outburst disaster

Coal and gas outburst disasters are the result of the simultaneous release of coal deformation energy and gas expansion energy (Guo et al. 2021b; Lei et al. 2022). Therefore, highly fractured tectonic coal and high gas pressure in coal seams are necessary conditions for coal and gas outbursts to occur. Analysis of the differences in gas occurrence in each coal seam of the Luling coal mine reveals that the thick eighth and ninth coal seams, which have undergone complex geological evolution, have formed a large number of tectonic coals. During the crushing process, these coal bodies generate a large amount of gas storage space, resulting in the accumulation of a large amount of gas in the coal body, providing favorable conditions for coal and gas outburst disasters.

For coal seams deposited during the Carboniferous-Permian period in China, gas management work should pay more attention to small-scale structural areas of coal seams (such as small faults and coal thickness variations). These areas are prone to the formation of large numbers of tectonic coal and a large amount of gas. For extremely high gas accumulation areas, comprehensive measures (Wang et al. 2023) such as protective layer depressurization, surface drilling for gas extraction, and "fluidization" depressurization through cross-layer drilling should be adopted according to the nature of the tectonic coal to actively release coal deformation energy and gas expansion energy, thereby reducing the risk of coal seam outbursts.

6 Conclusions

Based on the restoration of gas accumulation history, basic tests, and field investigations, the reasons for the differences in gas occurrence in the coal seam group in the Luling coal mine have been determined. A comprehensive analysis of macro and micro aspects reveals significant changes in these coal seams. The following conclusions can be summarized:

1) The oxygen-containing functional groups in coal play a crucial role in methane adsorption. The proportions of these functional groups in the Nos. 8, 9, and 10 coal seams are 61.9%, 62.3%, and 64%, respectively. The No. 10 coal seam has a larger proportion of oxygen-containing functional groups compared to the other seams, making gas adsorption less favorable in this seam.

2) Micropores and mesopores are essential for gas storage in coal seams. In the case of the Nos. 8 and 9 coal seams, these seams exhibit a substantial proportion of micropores and mesopores, with the maximum proportion reaching 50%. However, the No. 10 coal seam has a poorly developed micropore structure, accounting for only 22% of the pore volume. The presence and abundance of micropores and mesopores contribute significantly to the gas storage limit of coal seams. Hence, the Nos. 8 and 9 coal seams have high gas reserves.

3) The gas adsorption capacity depends on the proportion of pores capable of adsorbing gas. Due to the lower proportion of favorable adsorption pores in the No. 10 coal seam, its gas adsorption capacity is significantly lower compared to the Nos. 8 and 9 coal seams. The limit gas adsorption capacities for the three coal seams (0.2–0.25 mm) are 43.09 m^3/t, 36.61 m^3/t, and 20.61 m^3/t, respectively. The Nos. 8 and 9 seams exhibit greater gas storage capacity in the identical external environment, and the storage potential escalates as the seams undergo increased crashing.

4) There are notable differences in the degree of coal crushing between each coal seam. The tectonic coal in the Nos. 8 and 9 coal seams is broken into smaller particle sizes, which

are more widely distributed. This fragmentation of coal enhances the storage capacity of gas compared to the No. 10 coal seam. Additionally, the roof of the Nos. 8 and 9 coal seams consists of extremely thick mudstone, which provides better sealing compared to the sandstone roof of the No. 10 coal seam. The improved sealing effect of the roof in the Nos. 8 and 9 coal seams further facilitates the storage of gas in these seams.

Declarations

Conflict of interest The authors have no relevant financial or non-financial interests to disclose.

References

Bustin RM, Clarkson CR (1998) Geological controls on coalbed methane reservoir capacity and gas content. Int J Coal Geol 38:3–26. https://doi.org/10.1016/S0166-5162(98)00030-5

Cai P, Nie W, Chen D, Yang S, Liu Z (2019) Effect of air flowrate on pollutant dispersion pattern of coal dust particles at fully mechanized mining face based on numerical simulation. Fuel 239:623–635. https://doi.org/10.1016/j.fuel.2018.11.030

Chen Y, Mastalerz M, Schimmelmann A (2012) Characterization of chemical functional groups in macerals across different coal ranks via micro-FTIR spectroscopy. Int J Coal Geol 104:22–33. https://doi.org/10.1016/j.coal.2012.09.001

Cheng X, Zhao G, Li Y, Meng X, Tu Q (2020) Key technologies and engineering practices for soft-rock protective seam mining. Int J Min Sci Technol 30:889–899. https://doi.org/10.1016/j.ijmst.2020.07.006

Cheng Y, Liu Q, Ren T (2021) Coal mechanics. Springer Singapore, Singapore. https://doi.org/10.1007/978-981-16-3895-4

Ding D, Liu G, Fu B (2019) Influence of carbon type on carbon isotopic composition of coal from the perspective of solid-state C-13 NMR. Fuel 245:174–180. https://doi.org/10.1016/j.fuel.2019.02.072

Fu S, Wang L, Li S, Zheng S, Li J (2023) The effect of organic matter fraction extracted on micropores development degree and CH4 adsorption capacity of coal. Gas Sci Eng 110:204870. https://doi.org/10.1016/j.jgsce.2022.204870

Fu S, Wang L, Li S, Ni S, Cheng Y, Zhang X, Liu S (2024) Re-thinking methane storage mechanism in highly metamorphic coalbed reservoirs — a molecular simulation considering organic components. Energy 293:130444. https://doi.org/10.1016/j.energy.2024.130444

Guo H, Tang H, Wu Y, Wang K, Xu C (2021a) Gas seepage in underground coal seams: application of the equivalent scale of coal matrix-fracture structures in coal permeability measurements. Fuel 288:119641. https://doi.org/10.1016/j.fuel.2020.119641

Guo H, Wang K, Wu Y, Tang H, Wu J, Guan L, Chang C, Xu C (2021b) Evaluation of the weakening behavior of gas on the coal strength and its quantitative influence on the coal deformation. Int J Min Sci Technol 31:451–462. https://doi.org/10.1016/j.ijmst.2021.03.005

Jiang B, Qu Z, Wang GGX, Li M (2010) Effects of structural deformation on formation of coalbed methane reservoirs in Huaibei coalfield, China. Int J Coal Geol 82:175–183. https://doi.org/10.1016/j.coal.2009.12.011

Karacan CO, Goodman GVR (2012) Analyses of geological and hydrodynamic controls on methane emissions experienced in a lower Kittanning coal mine. Int J Coal Geol 98:110–127. https://doi.org/10.1016/j.coal.2012.04.002

Karacan CO, Ruiz FA, Cote M, Phipps S (2011) Coal mine methane: a review of capture and utilization practices with benefits to mining safety and to greenhouse gas reduction. Int J Coal Geol 86:121–156. https://doi.org/10.1016/j.coal.2011.02.009

Kong S, Cheng Y, Ren T, Liu H (2014) A sequential approach to control gas for the extraction of multi-gassy coal seams from traditional gas well drainage to mining-induced stress relief. Appl Energy 131:67–78. https://doi.org/10.1016/j.apenergy.2014.06.015

Lei Y, Cheng Y, Wang L, Ren T, Li Q (2022) Potential infrasonic tremors in coal seam systems: implications for the prediction of coal and gas outbursts. Fuel 326:125000. https://doi.org/10.1016/j.fuel.2022.125000

Li Y, Shao L, Fielding CR, Wang D, Mu G (2021) Sequence stratigraphy, paleogeography, and coal accumulation in a lowland alluvial plain, coastal plain, and shallow-marine setting: Upper carboniferous-Permian of the Anyang-Hebi coalfield, Henan Province, North China. Palaeogeogr Palaeoclimatol Palaeoecol 567:110287. https://doi.org/10.1016/j.palaeo.2021.110287

Liu J, Zhang R, Song D, Wang Z (2019) Experimental investigation on occurrence of gassy coal extrusion in coalmine. Saf Sci 113:362–371. https://doi.org/10.1016/j.ssci.2018.12.012

Moore TA (2012) Coalbed methane: a review. Int J Coal Geol 101:36–81. https://doi.org/10.1016/j.coal.2012.05.011

Pashin JC (2007) Hydrodynamics of coalbed methane reservoirs in the Black Warrior Basin: key to understanding reservoir performance and environmental issues. Appl Geochem 22:2257–2272. https://doi.org/10.1016/j.apgeochem.2007.04.009

Qin Y, Moore TA, Shen J, Yang Z, Shen Y, Wang G (2018) Resources and geology of coalbed methane in China: a review. Int Geol Rev 60:777–812. https://doi.org/10.1080/00206814.2017.1408034

Shao L, Dong D, Li M, Wang H, Wang D, Lu J, Zheng M, Cheng A (2014) Sequence-paleogeography and coal accumulation of the Carboniferous-Permian in the North China Basin. J China Coal Soc 39:1725–1734. https://doi.org/10.13225/j.cnki.jccs.2013.9033

Staub JR, Cohen AD (1979) The Snuggedy Swamp of South Carolina: A Back-Barrier Estuarine Coal-Forming Environment. SEPM J Sediment Res Vol 49. https://doi.org/10.1306/212F76D5-2B24-11D7-8648000102C1865D

Su XB, Zhang LP, Zhang RL (2003) The abnormal pressure regime of the Pennsylvanian 8 coalbed methane reservoir in Liulin-Wupu District, Eastern Ordos Basin, China. Int J Coal Geol 53:227–239. https://doi.org/10.1016/S0166-5162(03)00015-6

Sun Y, Wang L, Wang R, Zheng S, Liao X, Zhu Z, Zhao Y (2022) Insight on microscopic mechanisms of CH4 and CO2 adsorption of coal with different ranks. Fuel 330:125715. https://doi.org/10.1016/j.fuel.2022.125715

Suto N, Kawashima H (2016) Global mapping of carbon isotope ratios in coal. J Geochem Explor 167:12–19. https://doi.org/10.1016/j.gexplo.2016.05.001

Thommes M, Kaneko K, Neimark AV, Olivier JP, Rodriguez-Reinoso F, Rouquerol J, Sing KSW (2015) Physisorption of gases, with special reference to the evaluation of surface area and pore size distribution (IUPAC Technical Report). Pure Appl Chem 87:1051–1069. https://doi.org/10.1515/pac-2014-1117

Wang C, Cheng Y (2023) Role of coal deformation energy in coal and gas outburst: a review. Fuel 332:126019. https://doi.org/10.1016/j.fuel.2022.126019

Wang L, Cheng Y, Wang, Lei, Guo P, Li W (2012) Safety line method for the prediction of deep coal-seam gas pressure and its application in coal mines. Saf Sci 50:523–529. https://doi.org/10.1016/j.ssci.2011.09.022

Wang H, Cheng Y, Yuan L (2013) Gas outburst disasters and the mining technology of key protective seam in coal seam group in the Huainan coalfield. Nat Hazards 67:763–782. https://doi.org/10.1007/s11069-013-0602-5

Wang H, Zhang L, Wang D, He X (2017) Experimental investigation on the wettability of respirable coal dust based on infrared spectroscopy and contact angle analysis. Adv Powder Technol 28:3130–3139. https://doi.org/10.1016/j.apt.2017.09.018

Wang L, Sun Y, Zheng S, Shu L, Zhang X (2023) How efficient coal mine methane control can benefit carbon-neutral target: evidence from China. J Clean Prod 424:138895. https://doi.org/10.1016/j.jclepro.2023.138895

Zheng G, Ma X, Guo Z, Hilton DR, Xu W, Liang S, Fan Q, Chen W (2017) Gas geochemistry and methane emission from Dushanzi mud volcanoes in the southern Junggar Basin, NW China. J Asian Earth Sci 149:184–190. https://doi.org/10.1016/j.jseaes.2017.08.023

Zhu G, Gu L, Su J, Dai J, Ding W, Zhang J, Song L (2012) Sedimentary association of alternated mudstones and tight sandstones in China's oil and gas bearing basins and its natural gas accumulation. J Asian Earth Sci 50:88–104. https://doi.org/10.1016/j.jseaes.2012.01.008